ceramics

Article

Prediction of Physical and Mechanical Properties of Al_2O_3–TiB_2–TiC Composites Using Design of Mixture Experiments

Nestor Washington Solís Pinargote [1,2,*], Yuri Pristinskiy [1,2], Yaroslav Meleshkin [1,2], Alexandra Yu. Kurmysheva [1], Aleksandr Mozhaev [2], Nikolay Lavreshin [2,3] and Anton Smirnov [1,2,*]

1 Laboratory of Electric Current Assisted Sintering Technologies, Moscow State University of Technology "STANKIN", Vadkovsky per. 1, 127055 Moscow, Russia; y.pristinskiy@stankin.ru (Y.P.); ya.meleshkin@stankin.ru (Y.M.); aukurm@gmail.com (A.Y.K.)
2 Department of High-Efficiency Machining Technologies, Moscow State University of Technology "STANKIN", Vadkovsky per. 1, 127055 Moscow, Russia; a.mozhaev@stankin.ru (A.M.); n.lavreshin@stankin.ru (N.L.)
3 Microbor, SEZ Technopolis, Volgogradsky Ave. 42k5, 5-23H, 109316 Moscow, Russia
* Correspondence: nw.solis@stankin.ru (N.W.S.P.); a.smirnov@stankin.ru (A.S.); Tel.: +7-499-972-95-85 (N.W.S.P.)

Abstract: In this study, the design of mixture experiments was used to find empirical models that could predict, for a first approximation, the relative density, flexural strength, Vickers hardness and fracture toughness of sintered composites in order to identify further areas of research in the Al_2O_3-TiB_2-TiC ternary system. The composites were obtained by spark plasma sintering (SPS) of these mixtures at 1700 °C, 80 MPa and a dwell of 3 min. The obtained experimental results were analyzed in the statistical analysis software Minitab 17, and then, different regression models were obtained for each property. Based on the selected models, contour plots were made in the Al_2O_3–TiB_2–TiC simplex for a visual representation of the predicted results. By combining these plots, it was possible to obtain one common zone in the Al_2O_3–TiB_2–TiC simplex, which shows the following combination of physical and mechanical properties for sintered samples: relative densities, flexural strength, Vickers hardness, and fracture toughness of than 99%, 500 MPa, 18 GPa, and 7.0 MPa·m$^{1/2}$, respectively. For a first approximation in determining the further area of research, the obtained models describe well the behavior of the studied properties. The results of the analysis showed that the design of mixture experiments allows us to identify the most promising compositions in terms of mechanical properties without resorting to labor-intensive and financially expensive full-scale experiments. Our work shows that 10 different compositions were required for preliminary analysis.

Keywords: design of mixture experiments; ceramics; spark plasma sintering; Al_2O_3; TiC; TiB_2; composites; relative density; flexural strength; fracture toughness; Vickers hardness

check for updates

Citation: Solís Pinargote, N.W.; Pristinskiy, Y.; Meleshkin, Y.; Kurmysheva, A.Y.; Mozhaev, A.; Lavreshin, N.; Smirnov, A. Prediction of Physical and Mechanical Properties of Al_2O_3–TiB_2–TiC Composites Using Design of Mixture Experiments. *Ceramics* **2024**, *7*, 1639–1657. https://doi.org/10.3390/ceramics7040105

Academic Editor: Frederic Monteverde

Received: 23 September 2024
Revised: 25 October 2024
Accepted: 29 October 2024
Published: 7 November 2024

1. Introduction

In the past few decades, ceramic materials such as alumina (Al_2O_3), titanium carbide (TiC), and titanium diboride (TiB_2) have been attracting more and more attention and have greater application as key components of ceramic tool materials, due to their excellent properties such as high hardness, strength, as well as high wear, corrosion, and heat resistances [1]. Nevertheless, the application of single phases of these ceramic materials is limited by their poor fracture toughness and variability in their mechanical strength.

Some scholars have reported that composites based on these phases have higher hardness, flexural strength, and fracture toughness compared to monolithic materials. The ternary composite materials based on Al_2O_3–TiB_2–TiC are commonly produced by self-propagating high temperature synthesis (SHS) [2], laser-assisted SHS [3], hot pressing (HP) [4–6], or spark plasma sintering (SPS) [7]. The results of these works indicate that mechanical properties of these ternary composites are superior to those of their single-phase materials, and even to those of the binary composites based on Al_2O_3–TiC [8]; Al_2O_3–TiB_2 [9]; TiB_2–TiC [10].

Al_2O_3–TiB_2–TiC-based composite materials may have a variety of characteristics, depending on which phase is the main component. For instance, high alumina content would lead to a composite material for corrosion applications that shows higher fracture toughness, superior mechanical strength, and better oxidation and impact resistance. On the other hand, composites based on TiC or TiB_2 could be used for tribological and electrical applications, due to their enhanced wear resistance and electrical conductivity [11]. Thus, composites based on the Al_2O_3–TiB_2–TiC system, due to their improved properties, are attractive for advanced applications as wear-resistant coatings [12–14], strengthening of metal–ceramic composites [11,15,16], ceramic cutting tools [4–6,17], and as self-lubricating ceramic tool material [18]. Thereby, the preliminary determination of the physical and mechanical properties of compositions within the ternary diagram Al_2O_3–TiB_2–TiC is necessary to establish a rational choice of composite composition depending on the intended application.

To prevent the change of the TiB_2 phase into titanium (TiO_2) and boron (B_2O_3) oxides due to prolonged high temperatures in the presence of aluminum oxide, as well as to achieve high density values, it is necessary to use a sintering technology that will ensure a high heating rate with simultaneous mechanical pressing. SPS technology can provide high heating rates (from 100 °C/min to 1000 °C/min) that allow the conventional long process of sintering materials to be transformed into a fast and short process, in which uncontrolled grain growth is reduced or eliminated [19–23]. Furthermore, the application of external mechanical pressure during heating permits high density values of sintered materials with better mechanical properties [24,25]. However, full-scale experiments are expensive and time-consuming, so alternative methods are needed.

The design of mixture experiments is a method which uses statistical concepts applied to mixture problems to find relations between chemical constituents as the factors and mixture properties as the responses in order to identify the behavior of each component in the mixture environment [26]. Once relationships are established, which is commonly completed through mathematical models, they can be used to describe, predict, or explain results, as well as to optimize compositions [27]. According to the design of mixture experiments, to obtain a linear mathematical model of a ternary system, only three experimental points are necessary; adding three other experimental points, it is possible to establish a second order polynomial, and a reduced cubic model can be calculated with one more experimental point [27]. This shows that the design of mixture experiments is a good tool to establish the relationships between factors and the responses using a minimum number of trials in the mixture environment.

This approach is sometimes used to predict the physical and mechanical properties of ceramic composites in the first approximation with the aim of further optimization of the composition depending on the required properties of the study. For example, de Mestral and Thevenot showed in their research [28–30] how, using the design of mixture experiments, they could predict the tensile strength, hardness, fracture toughness, and electrical conductivity of boride–carbide composites. In addition, other research groups used this method to predict the other properties of ceramic composites, such as water absorption, flexural strength, open porosity, linear firing shrinkage, weight loss, density, hardness, friction, and wear behavior [31–34].

The aim of this work was to establish mathematical models that could predict, for a first approximation, the relative density, flexural strength, Vickers hardness, and fracture toughness of sintered composites in order to identify further areas of research in the Al_2O_3–TiB_2–TiC ternary system. The established models could be used for the elaboration of contour plots in the Al_2O_3–TiB_2–TiC ternary diagram for a visual representation of the predicted results and for the rapid identification of zones or compositions with specific required properties.

2. Materials and Methods

2.1. Powder Mixture Preparation

In this study, three different commercial ceramic powders, Al_2O_3 (purity 99.9%), TiB_2 (purity 99.9%), and TiC (purity 99.5%), produced by "Plasmotherm" Ltd., Moscow, Russia, were used.

A {3,2} centroid simplex-lattice design (Figure 1), augmented with interior points, was generated in Minitab 17 in order to define the composition of the necessary mixtures that should be investigated in this work. The expression {q,m} specifies that this design can support a polynomial model of degree "m" using "q" components in the simplex-lattice [19]. Moreover, the number "m" is used to determine "m + 1" equal proportions of each component that vary from 0 to 1, and which are calculated as follows:

$$x_i = 0,\ \frac{1}{m},\ \frac{2}{m},\ \ldots,\ 1.$$

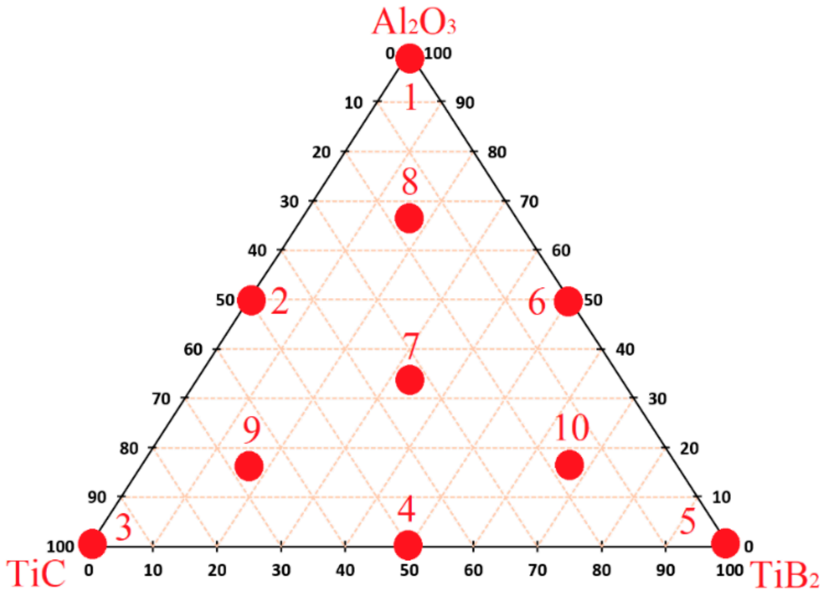

Figure 1. Centroid simplex-lattice design used for the Al_2O_3–TiB_2–TiC system.

In this way, {3,2} indicates that it is possible to obtain a second-degree model, which can represent the response surface over the entire simplex region consisting of 3 components with the use of 3 equal proportions for each of them (0, 1/2, 1). Thus, the points of the {3,2} simplex-lattice are

$$(x_1,\ x_2,\ x_3) = (1,\ 0,\ 0),\ (1/2, 1/2, 0),\ (0,\ 1,\ 0), (0,\ 1/2, 1/2), (0,\ 0,\ 1), (1/2, 0, 1/2)$$

that correspond to points No. 1, 2, 3, 4, 5, 6 of this work (Figure 1), respectively. The notations x_1, x_2, x_3 represent the proportions of Al_2O_3, TiC, and TiB_2, respectively.

Furthermore, a central point (No. 7, Figure 1) and three testing points (No. 8–10, Figure 1) were included in the {3,2} simplex-lattice, with the aim to design an augmented {3,2} centroid simplex-lattice.

These 10 points in the ternary plot Al_2O_3–TiB_2–TiC show the coordinates of each mixture, and their coordinates indicate the amount-of-substance fraction in molar % (Table 1).

For every mixture, the proportions of each raw powder materials, listed in Table 1, were added to a polyethylene jar. Al_2O_3 balls (∅3 mm) were then added to the jar with powders at a ball-to-powder weight ratio of 3:1. Isopropanol, as the liquid medium, was then also added to the jar at an isopropanol-to-powder weight ratio of 1:1. Next, the polyethylene jars were tightly sealed and placed in a ball mill to grind and mix the components of each powder mixture for 36 h of use. After this time, the obtained wet mixtures were dried in a vacuum drying oven for 12 h at 80 °C. Finally, the dried mixtures were crushed in an agate mortar and then sifted through a 63-micron sieve.

Table 1. Coordinates of mixtures in the ternary plot Al_2O_3–TiB_2–TiC.

Point	Al_2O_3	TiC	TiB_2	Mixture
No.		[mol %]		Name
1	100.00	0.00	0.00	ATB-1
2	50.00	50.00	0.00	ATB-3
3	0.00	100.00	0.00	ATB-5
4	0.00	50.00	50.00	ATB-7
5	0.00	0.00	100.00	ATB-9
6	50.00	0.00	50.00	ATB-11
7	33.33	33.33	33.33	ATB-22
		Test points		
8	67.00	16.50	16.50	ATB-13
9	16.50	67.00	16.50	ATB-16
10	16.50	16.50	67.00	ATB-19

2.2. Spark Plasma Sintering

All powder mixtures were sintered in a Spark Plasma Sintering Machine H-HP D 25 SD from FCT Systeme GmbH (Rauenstein, Germany), and disc composites with a diameter of 40 mm and 4 mm in height were obtained. The sintering process started with the application of a pressure of 47 MPa that was maintained from room temperature up to 300 °C. After that, both pressure and temperature grew continuously up to 80 MPa and 1600 °C, respectively. Heating from room temperature up to 1600 °C was conducted by a heating rate of 100 °C/min. After reaching 1600 °C the heating rate was reduced to 25 °C/min to reach the sintering temperature of 1700 °C which was maintained for 3 min. When heating finished, samples were cooled naturally in the sintering chamber. Figure 2 shows the applied force and temperature schedules, as well as the punch displacement behavior as a function of time during the SPS process. From each powder mixture, three sintered samples were obtained, in which the measurements of relative density and flexural strength were carried out for statistical analysis.

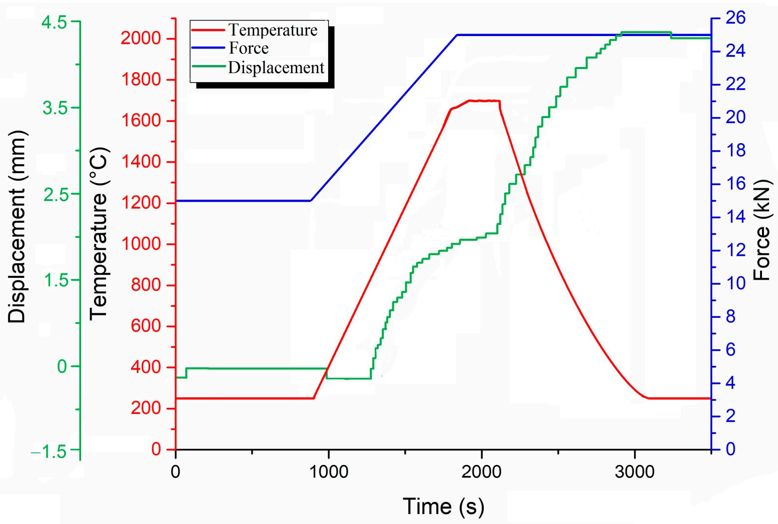

Figure 2. The applied force and temperature schedules and punch displacement behavior during SPS process.

2.3. Relative Densities Measurement

Archimedes' method was used for measuring the sintered composite densities in distilled water. For each mixture, the relative density was calculated as the ratio of its measured density over the calculated theoretical density. Theoretical densities were calculated according to the rule of mixtures assuming densities of 3.94 g/cm^3 for Al_2O_3, 4.85 g/cm^3 for TiC, and 4.35 g/cm^3 for TiB_2, which were measured by an AccuPyc II 1340 helium pycnometer (Micrometrics, Norcross, GA, USA).

2.4. Flexural Strength Testing

Flexural strength was determined following the standard [35] using a displacement rate of 0.5 mm/min in an ElectroPuls E10000 universal testing machine (Instron, High Wycombe, UK) by three-point bend tests, with a span of 20 mm. The samples for the tests were bars with a cross section of 2.0 mm × 1.5 mm and length of at least 25 mm. In this regard, the end surfaces of the sintered discs with a diameter of 40 mm and a height of 4 mm were initially flat grinded, in order to achieve three goals: removing the defective layer, achieving a disc thickness of 2 mm, and flat parallelism of the machined surfaces. In addition, due to the fact that the TiB_2 and TiC phases are electrically conductive, most of the sintered discs have sufficient electrical conductivity for wire electrical discharge machining (WEDM). Therefore, the electrically conductive discs were processed on a WEDM machine, and those discs that did not have sufficient electrical conductivity were processed on a precision cutting machine Accutom 50 (Struers GmbH, Ballerup, Denmark) using a diamond disc. Figure 3 shows the WEDM process of conductive specimens.

(**a**) (**b**)

Figure 3. Wire electrical discharge machining process of conductive discs: (**a**) installation of a block of 3 discs on the WEDM machine; (**b**) result of WEDM process of the first bars.

After WEDM of disks, the resulting bars were assembled and glued onto a metal substrate, and then the electrical discharge machining surfaces were flat grinded in order to remove defects on them, as well as to achieve plane parallelism and a size of 1.5 mm.

Figure 4 shows the sample reparation process of conductive specimens for the flat grinding. Figure 4a demonstrates the preparation and classification of obtained bars for gluing. Figure 4b shows the gluing process of bars to a metal substrate, while in Figure 4c, the flat grinding process of bars is exhibited.

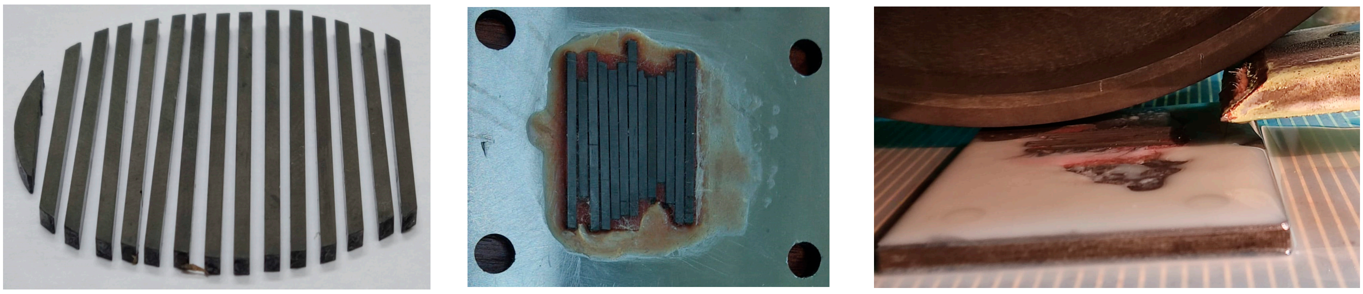

(a) (b) (c)

Figure 4. The process of surface grinding of samples: (**a**) bars obtained after electrical discharge machining of disks; (**b**) gluing bars to a metal substrate; (**c**) the process of grinding bars.

After flat grinding, the bars were ground and polished before testing, and four edges on the tensile surface were chamfered to an angle of 45° in order to eliminate a failure initiated from the edge of the specimen. For each composition, 3 samples were tested, and the mean value of the test results was calculated.

2.5. Vickers Hardness Testing

The sintered samples were polished before the hardness measuring. The indentation method was implemented for measuring the Vickers hardness (Hv) of samples. The measuring process was carried out in a microhardness tester (Qness, Salzburg, Austria) with a standard diamond pyramid indenter, under a load of 98 N for 10 s. In each sample, 10 indentations were made, and then the arithmetic mean for each composition was calculated. The Equation used for the hardness calculation was

$$HV = 0.1891\, P/d^2,$$

where P is the set load (N), and d is the average length of two diagonals (mm).

2.6. Fracture Toughness Testing

Fracture toughness of the polished samples was measured by the microindentation method with an applied load of 98 N for 10 s. Fracture toughness was calculated using the formula given by Miranzo and Moya as was indicated in our previous work [1].

2.7. X-Ray Diffraction (XRD) Analysis

The determination of the phase composition of the sintered composites was carried out on an Empyrean X-ray diffractometer (PANalytical, Almelo, The Netherlands), in the following modes: Cu-Kα spectrum, wavelength 1.5405981 Å, voltage 60 kV, beam current 30 mA, in a 2θ range from 20° to 65°, and step size 0.05°.

3. Results

3.1. X-Ray Diffraction (XRD)

Figure 5 shows the XRD pattern of sintered composites from mixtures listed in Figure 1: ATB-1 (a), ATB-3 (b), ATB-5 (c), ATB-7 (d), ATB-9 (e), ATB-11 (f), ATB-13 (g), ATB-16 (h), ATB-19 (i), ATB-22 (j).

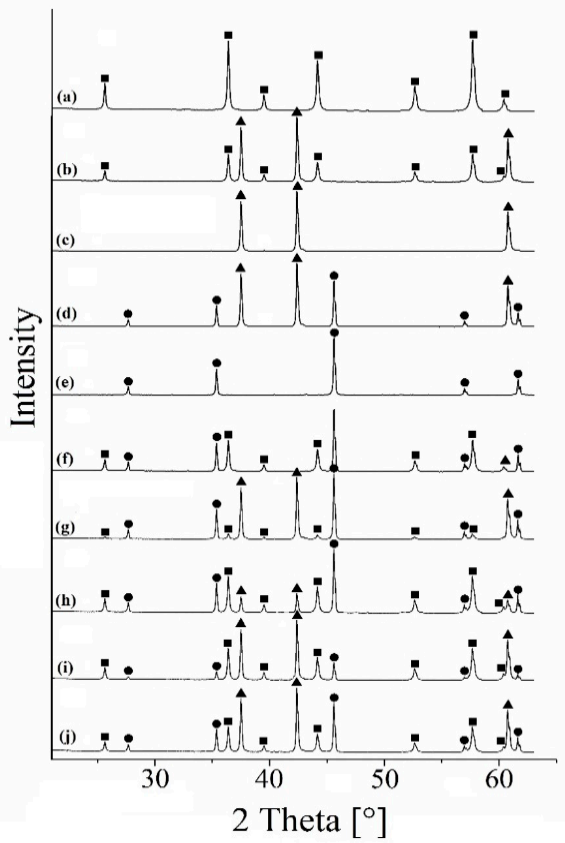

Figure 5. XRD pattern of sintered composites from mixtures: ATB-1 (a), ATB-3 (b), ATB-5 (c), ATB-7 (d), ATB-9 (e), ATB-11 (f), ATB-13 (g), ATB-16 (h), ATB-19 (i), ATB-22 (j). The triangles indicate the peaks of titanium carbide, the circles indicate the peaks of titanium diboride, and the squares indicate the peaks of aluminum oxide.

3.2. Relative Densities of Sintered Composites

Table 2 shows the calculated theoretical densities for each powder mixture, as well as the measured relative densities of sintered composites.

Table 2. Relative densities of sintered composites.

Point No.	Mixture	$\rho_{th.}$ * [g/cm^3]	Replication 1	Replication 2	Replication 3	Average Density
			ρ_{rel}, [%] *			ρ_{rel}, [%] *
1	ATB-1	3.950	97.53	96.69	98.36	97.53 ± 0.84
2	ATB-3	4.241	97.32	97.42	96.11	96.95 ± 0.73
3	ATB-5	4.850	94.52	93.52	93.79	93.94 ± 0.52
4	ATB-7	4.568	99.47	99.87	99.96	99.77 ± 0.26
5	ATB-9	4.350	99.35	98.20	98.70	98.75 ± 0.58
6	ATB-11	4.103	99.64	98.44	99.78	99.29 ± 0.74
7	ATB-22	4.334	98.89	97.95	98.31	98.38 ± 0.47
Test points						
8	ATB-13	4.109	98.67	98.32	97.63	98.21 ± 0.53
9	ATB-16	4.498	98.86	99.61	99.96	99.48 ± 0.56
10	ATB-19	4.285	98.54	99.82	98.48	98.95 ± 0.76

*: $\rho_{th.}$—calculated theoretical density; ρ_{rel}—relative density.

3.3. Flexural Strength

The flexural strength test results are presented in Table 3.

Table 3. Flexural strength of sintered composites.

Point	**Mixture**	**Replication**			**Average Flexural Strength**
		1	**2**	**3**	
No.			**σf, Mpa ***		**σf, Mpa ***
1	ATB-1	259.01	272.20	309.11	280.11 ± 25.97
2	ATB-3	460.05	507.42	409.23	458.90 ± 49.11
3	ATB-5	246.71	227.91	298.23	257.62 ± 36.41
4	ATB-7	532.86	561.88	639.03	577.92 ± 54.87
5	ATB-9	510.15	650.72	496.86	552.58 ± 85.25
6	ATB-11	399.75	447.12	410.28	419.05 ± 24.87
7	ATB-22	374.37	336.49	423.06	377.97 ± 43.40
			Test points		
8	ATB-13	351.83	413.64	474.68	413.38 ± 61.43
9	ATB-16	499.69	535.16	441.13	491.99 ± 47.49
10	ATB-19	601.10	670.64	637.39	636.38 ± 34.78

*: σf—measured flexural strength.

3.4. Vickers Hardness

Table 4 shows the measured Vickers hardness of each sintered sample.

Table 4. Vickers hardness of sintered composites.

Point	**Mixture**	**Replication**			**Average Vickers Hardness**
		1	**2**	**3**	
No.			**HV, Gpa ***		**HV, Gpa ***
1	ATB-1	15.2	14.0	12.5	13.9 ± 1.4
2	ATB-3	16.2	15.7	14.5	15.5 ± 0.9
3	ATB-5	14.2	14.8	12.5	13.8 ± 1.2
4	ATB-7	17.5	16.5	16.8	16.9 ± 0.5
5	ATB-9	15.9	16.9	17.5	16.8 ± 0.8
6	ATB-11	17.8	16.6	18.9	17.8 ± 1.2
7	ATB-22	21.3	18.9	21.1	20.4 ± 1.3
			Test points		
8	ATB-13	16.4	18.1	16.9	17.1 ± 0.9
9	ATB-16	17.2	19.9	19.4	18.8 ± 1.4
10	ATB-19	17.3	17.7	20.2	18.4 ± 1.6

*: HV—Vickers hardness.

3.5. Fracture Toughness

The fracture toughness (K1c) test results are listed in Table 5.

Table 5. Fracture toughness of sintered composites.

Point	**Mixture**	**Replication**			**Average Fracture Toughness**
		1	**2**	**3**	
No.			**K1c, MPa·m$^{1/2}$ ***		**K1c, MPa·m$^{1/2}$ ***
1	ATB-1	5.3	5.6	4.7	5.2 ± 0.5
2	ATB-3	6.7	6.4	7.0	6.7 ± 0.3
3	ATB-5	5.4	5.6	6.2	5.7 ± 0.4
4	ATB-7	5.7	5.8	6.1	5.9 ± 0.2
5	ATB-9	7.5	7.9	6.8	7.4 ± 0.6
6	ATB-11	7.7	6.7	6.4	6.9 ± 0.7
7	ATB-22	7.0	7.6	7.8	7.5 ± 0.4

Table 5. *Cont.*

Point	Mixture	Replication			Average
		1	2	3	Fracture Toughness
No.		K1c, MPa·m$^{1/2}$ *			K1c, MPa·m$^{1/2}$ *
		Test points			
8	ATB-13	9.1	8.8	7.8	8.6 ± 0.7
9	ATB-16	6.9	6.1	7.1	6.7 ± 0.5
10	ATB-19	7.8	8.2	8.1	8.0 ± 0.2

*: K1c—fracture toughness.

4. Discussion

The XRD patterns of sintered composites show that only Al_2O_3, TiB_2, and TiC phases were detected in the samples without the presence of any new impurities and phases.

The results of relative density, flexural strength, Vickers hardness, and fracture toughness were processed in Minitab 17, which is a statistical analysis software which can help in determining different regression models and establishing which of them is the most appropriate for the prediction of the given properties.

4.1. Relative Density Models

Table 6 shows the regression models obtained after analysis of variance (ANOVA) of relative density. In this table, the abbreviation RD is related to relative density, while the subscripts L, Q, and SC are related to the type of model obtained: linear, quadratic, and special cubic, respectively.

Table 6. Regression models obtained after ANOVA for relative density.

Regression Model	Property Equation
Linear	RD_L = 98.06 X1 + 96.25 X2 + 100.06 X3
Quadratic	RD_Q = 97.76 X1 + 94.47 X2 + 98.82 X3 + 4.83 X1X2 + 13.32 X2X3
Special cubic	RD_{SC} = 97.43 X1 + 94.48 X2 + 98.49 X3+ 5.74 X1X2 + 3.88 X1X2 + 14.23 X2X3 − 14.4 X1X2X3

In these models, the variables X1, X2, and X3 are coded values for Al_2O_3, TiC, and TiB_2, respectively. The coded values were calculated as the molar % of each component from Figure 1, divided by 100 (X1 = Al_2O_3 mol%/100; X2 = TiC mol%/100; X3 = TiB_2 mol%/100).

The estimated coefficients of the linear regression model (RD_L) were significant since ANOVA indicated that their *p*-values were lower than 0.05. However, its obtained R-squared (R^2) and predicted R-squared (R^2pred) values were 37.78% and 18.52%, respectively.

On the other hand, in the quadratic regression model (RD_Q), the quadratic term X1X3 was excluded from the equation, because its *p*-value was 0.234. For this model, the obtained R^2 and R^2pred values were 72.95% and 63.86%, respectively. This indicates that RD_Q better fit the experimental data than RD_L.

The analysis of mixture design in terms of the special cubic model corroborated that the term X1X3 was not significant, because its *p*-value was 0.165 (higher than 0.05), and it should have been excluded from the model. Furthermore, this analysis showed that the cubic term X1X2X3 was also not significant (*p*-value = 0.430), and should also have been excluded from the model. As a result of the analysis, the obtained model RD_{SC} after exclusion of terms X1X3 and X1X2X3 took the form of a quadratic equation, coinciding with RD_Q. The R^2 and R^2pred values of the reduced RD_{SC} were similar to these values for the RD_Q model.

Through a comparison between the model and experimental data, we have assessed the goodness of fit of the RD_Q model using residual plots. Figure 6a is a plot of standardized residuals against fitted values. These residuals represent the difference between the value of experimental responses of each composite and the estimated/fitted value of the density as predicted by the regression RD_Q model. If the residuals are roughly normally distributed, around 95% of them should lie between the cut-off values of −2.0 and 2.0, which are presented as horizontal lines. Values lying far above or below these boundaries are outliers. In Figure 6a, two residuals stand out from the basic pattern of residuals, and this suggests they are outliers. Moreover, Figure 6b shows the fitted line plot, which demonstrates a linear relationship between experimental responses and fitted values. According to the R-square value and the fitted line plot in Figure 6b, we can consider the model as significant.

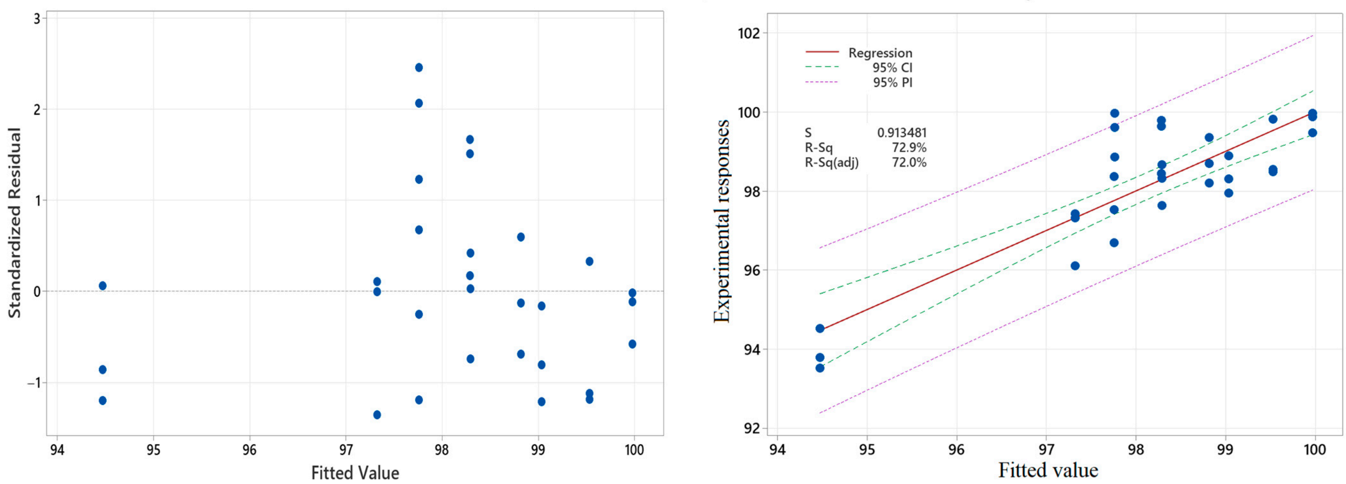

(**a**) (**b**)

Figure 6. Evaluation of quadratic model of relative density: (**a**) plot of standardized residual vs. fits, and (**b**) fitted line plot.

Based on the obtained results, it is possible to conclude that, as a first approximation, the behavior of the relative density of sintered samples in the ternary plot Al_2O_3–TiB_2–TiC could be modeled by the quadratic equation RD_Q.

4.2. Flexural Strength Models

Similarly, Table 7 shows the regression models obtained after ANOVA in relation to flexural strength. In these equations, the abbreviation FS is related to flexural strength, while the subscripts L, Q, and SC are related to the type of model obtained: linear, quadratic, and special cubic, respectively.

Table 7. Regression models obtained after ANOVA for flexural strength.

Regression Model	Property Equation
Linear	FS_L = 326.70 X1 + 390.80 X2 + 622.30 X3
Quadratic	FS_Q = 273.30 X1 + 270.30 X2 + 571.00 X3 + 623 X1X2 + 605 X2X3
Special cubic	FS_{SC} = 282.30 X1 + 264.10 X2 + 580.00 X3 + 760.00 X1X2 + 742.00 X2X3 − 2226.00 X1X2X3

The variables X1, X2, and X3 were calculated as indicated in Section 4.1.

In the linear regression model (FS_L), all the estimated coefficients were significant as their p-values were lower than 0.05. The obtained R^2 and R^2pred values of this regression model were 47.42% and 32.72%, respectively.

In the quadratic regression model (FS_Q), the quadratic term X1X3 was excluded from the equation, because its p-value was 0.617. For this model, the obtained R^2 and R^2pred values were 72.23% and 63.28%, respectively. This indicates that FS_Q better fit the experimental data than FS_L.

The analysis in terms of the special cubic model showed that the term X1X3 was not significant (p-value = 0.792), and it should have been excluded from the model. After exclusion of the term X1X3, the model FS_{SC} took the form shown in Table 7. The R^2 and R^2pred values of this FS_{SC} model were 76.01% and 63.74%, respectively. These values indicated that FS_{SC} fit the experimental data better than FS_Q.

Figure 7a shows the plot of standardized residuals against fitted values obtained from the special cubic model FS_{SC}. In this plot, only two residuals are outliers. Moreover, Figure 7b shows the fitted line plot of the FS_Q model, which demonstrates a linear relationship between experimental responses and fitted values. According to the R-square value and the fitted line plot shown in Figure 7b, we can consider the model as significant.

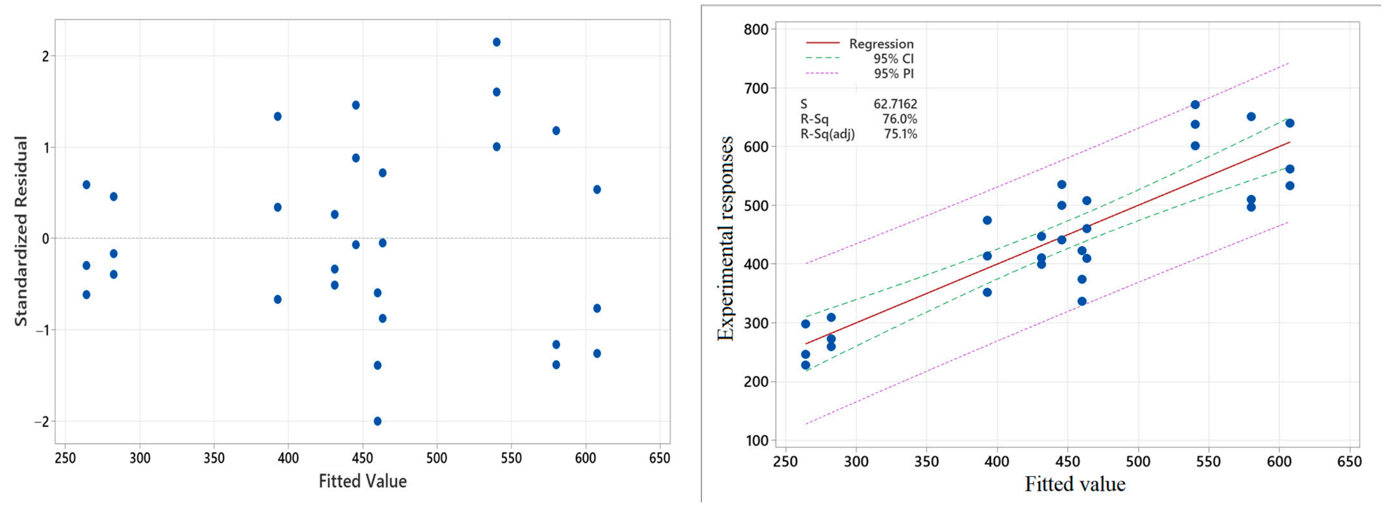

(**a**) (**b**)

Figure 7. Evaluation of special cubic model of flexural strength: (**a**) plot of standardized residual vs. fits, and (**b**) fitted line plot.

Based on the obtained results, it is possible to conclude that, as a first approximation, the behavior of the flexural strength of sintered samples in the ternary plot Al_2O_3–TiB_2–TiC could be modeled by the cubic model FS_{SC}.

4.3. Vickers Hardness Models

Table 8 shows the models obtained in relation to Vickers hardness (HV), while the subscripts L, Q, SC, and FC are related to the type of model obtained: linear, quadratic, special cubic, and full cubic, respectively.

Table 8. Regression models obtained after ANOVA for Vickers hardness.

Regression Model	Property Equation
Linear	HV_L = 15.92 X1 + 16.17 X2 + 18.75 X3
Quadratic	HV_Q = 13.55 X1 + 14.03 X2 + 16.37 X3+ 11.78 X1X2 + 13.92 X1X3 + 11.81 X2X3
Special cubic	HV_{SC} = 13.72 X1 + 14.20 X2 + 16.54 X3 + 6.78 X1X2 + 8.92 X1X3 + 6.81 X2X3 + 81.00 X1X2X3

The calculations of variables X1, X2, and X3 was indicated in Section 4.1.

Since the *p*-values of the estimated coefficients in the linear regression model (HV_L) were lower than 0.05, it can be determined that they are significant. The obtained R^2 and R^2pred values of HV_L were 15.09% and 0.00%, respectively. These values indicate that the linear model fit 6.83% with the experimental data, the model cannot predict new observations, and it cannot be considered for further research.

The HV_Q showed R^2 and R^2pred values of 63.64% and 45.27%, respectively. This indicates that this model fits the experimental data much better than HV_L, but not sufficiently. The *p*-values of the estimated coefficients in this model were lower than 0.05.

The analysis of the experimental data in terms of the special cubic model (HV_{SC}) showed higher values of R^2 and R^2pred were obtained (76.74% and 62.51%, respectively). This means that the HV_{SC} model fits the experimental data better than HV_Q.

The residual plot for the model HV_{SC} is shown in Figure 8a. This figure indicates that no residual is an outlier. The fitted line plot of the HV_{SC} model is demonstrated in Figure 8b, which shows a linear relationship between experimental responses and fitted values. According to the R-square value and the fitted line plot shown in Figure 8b, this model can be considered as significant.

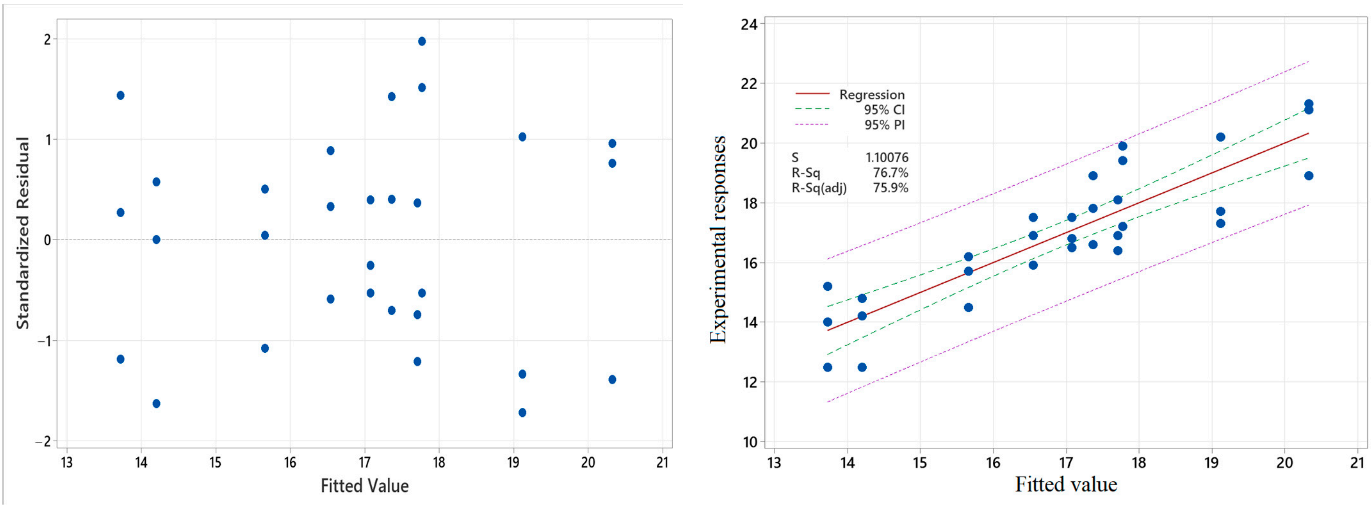

(**a**) (**b**)

Figure 8. Evaluation of special cubic model of Vickers hardness: (**a**) plot of standardized residual vs. fits, and (**b**) fitted line plot.

Based on the obtained results, it is possible to conclude that the behavior of the Vickers hardness of sintered samples in the ternary plot Al_2O_3–TiB_2–TiC could be modeled, as a first approximation, by the cubic model HV_{SC}.

4.4. Fracture Toughness Models

Table 9 shows the regression models obtained after ANOVA for fracture toughness, (FT), while the subscripts L, Q, SC, and FC are related to the type of model obtained: linear, quadratic, special cubic, and full cubic, respectively.

Table 9. Regression models obtained after ANOVA for fracture toughness.

Regression Model	Property Equation
Linear	FT_L = 6.73 X1 + 6.11 X2 + 7.74 X3
Quadratic	FT_Q = 5.45 X1 + 5.44 X2 + 7.30 X3+ 7.52 X1X2 + 5.50 X1X3
Special cubic	FT_{SC} = 5.53 X1 + 5.33 X2 + 7.19 X3 + 5.80 X1X2 + 3.78 X1X3 + 28.10 X1X2X3

The variables X1, X2, and X3 can be calculated as indicated in Section 4.1.

All the estimated coefficients in the linear regression model (FS_L) were significant. The obtained R^2 and R^2pred values of this regression model were 17.70% and 0.00%, respectively. These results indicate that this model fits the experimental data worst, and it cannot predict new observations. Thus, the FS_L model cannot be considered for further research.

The quadratic regression model (FT_Q) showed R^2 and R^2pred values of 55.60% and 37.16%, respectively. This indicates that FT_Q fits the experimental data much better than FT_L, but not sufficiently. In this model, the quadratic term X2X3 was excluded from the equation because its *p*-value was 0.713.

The analysis in terms of the special cubic model showed that the term X2X3 was not significant (*p*-value = 0.146), and should have been excluded from the model. After exclusion of the term X2X3, the model FS_{SC} took the form shown in Table 9. The R^2 and R^2pred values of this FT_{SC} model were 63.55% and 45.52%, respectively. These values indicated that FT_{SC} fit the experimental data better than FT_Q.

The comparison of the experimental data and fitted values from the FT_{SC} model for fracture toughness is presented in Figure 9a by the residual plot. From this figure, it can be seen that only two residuals are outliers. Moreover, Figure 9b shows a linear relationship between experimental responses and fitted values in the fitted line plot of the FT_{SC} model. According to the R-square value and the fitted line plot shown in Figure 9b, we can consider the model as significant.

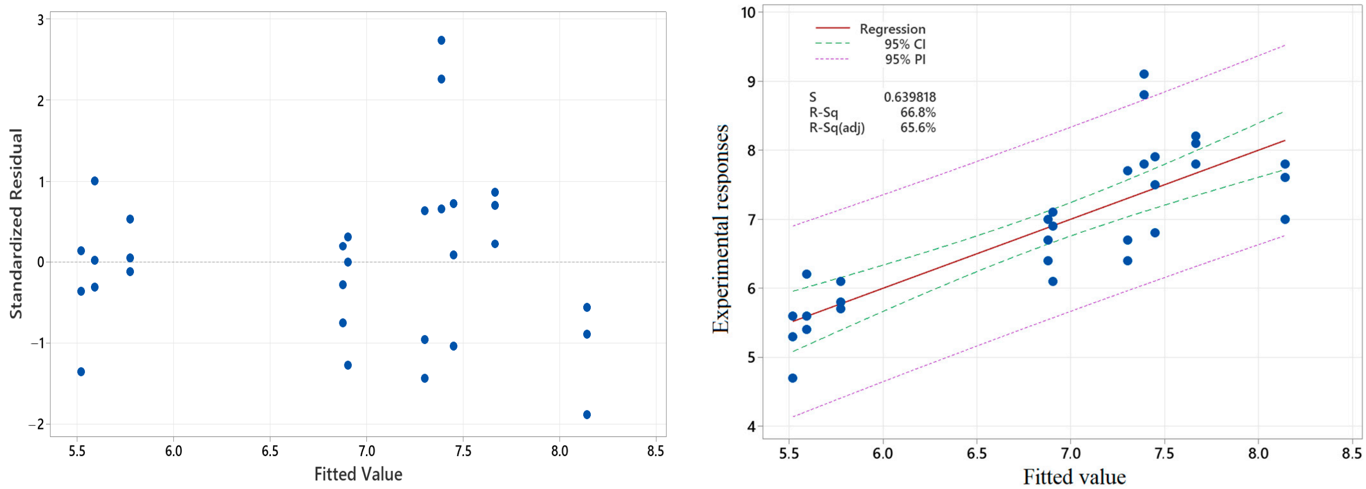

(**a**) (**b**)

Figure 9. Evaluation of special cubic model of fracture toughness: (**a**) plot of standardized residual vs. fits, and (**b**) fitted line plot.

Based on the obtained results, it is possible to conclude that the behavior of the fracture toughness of sintered samples in the ternary plot Al_2O_3–TiB_2–TiC could be modeled, as a first approximation, by the cubic model FT_{SC}.

4.5. Contour Plots

Based on the obtained equations RD_Q, FS_{SC}., HV_{SC}, and FT_{SC}, contour plots were made in the Al_2O_3-TiB_2-TiC simplex for a visual representation of the predicted results of the relative density, flexural strength, Vickers hardness, and fracture toughness of sintered samples (Figure 10).

Figure 10a shows the contour plot of relative density. From this figure, it can be noticed that the predicted zone with a density greater than 99% occupies an area which includes the points No. 4, 5, 7, and 10 (red numbers in the figure). According to this figure, the highest predicted values are found in the region between the points No. 4 and 5. Figure 10b shows the contour plot of flexural strength. The predicted zone with a flexural strength greater than 500 MPa occupies an area which includes the points No. 4, 5, and 10 and areas close to them. In this figure, it is possible to notice that values greater than 600 MPa are located in the region close to the points No. 4 and 5. Figure 10c shows the contour plot of Vickers hardness. Here, it can be noticed that predicted zone with a Vickers hardness greater than 18 GPa occupies an extended area, which includes the points No. 6, 7, 8, 9, and 10 and areas close to them. Moreover, the highest predicted values are found in the region close to point No. 7. Figure 10d shows the plot of the fracture toughness. The predicted zone with fracture toughness values greater than 7.00 $MPa \cdot m^{1/2}$ occupies an extended area, which includes the points No. 5, 6, 7, 8, 9, and 10 and areas close to them. Here it is noticed that values greater than 8.00 MPa·m$^{1/2}$ are located in the region close to point No. 7.

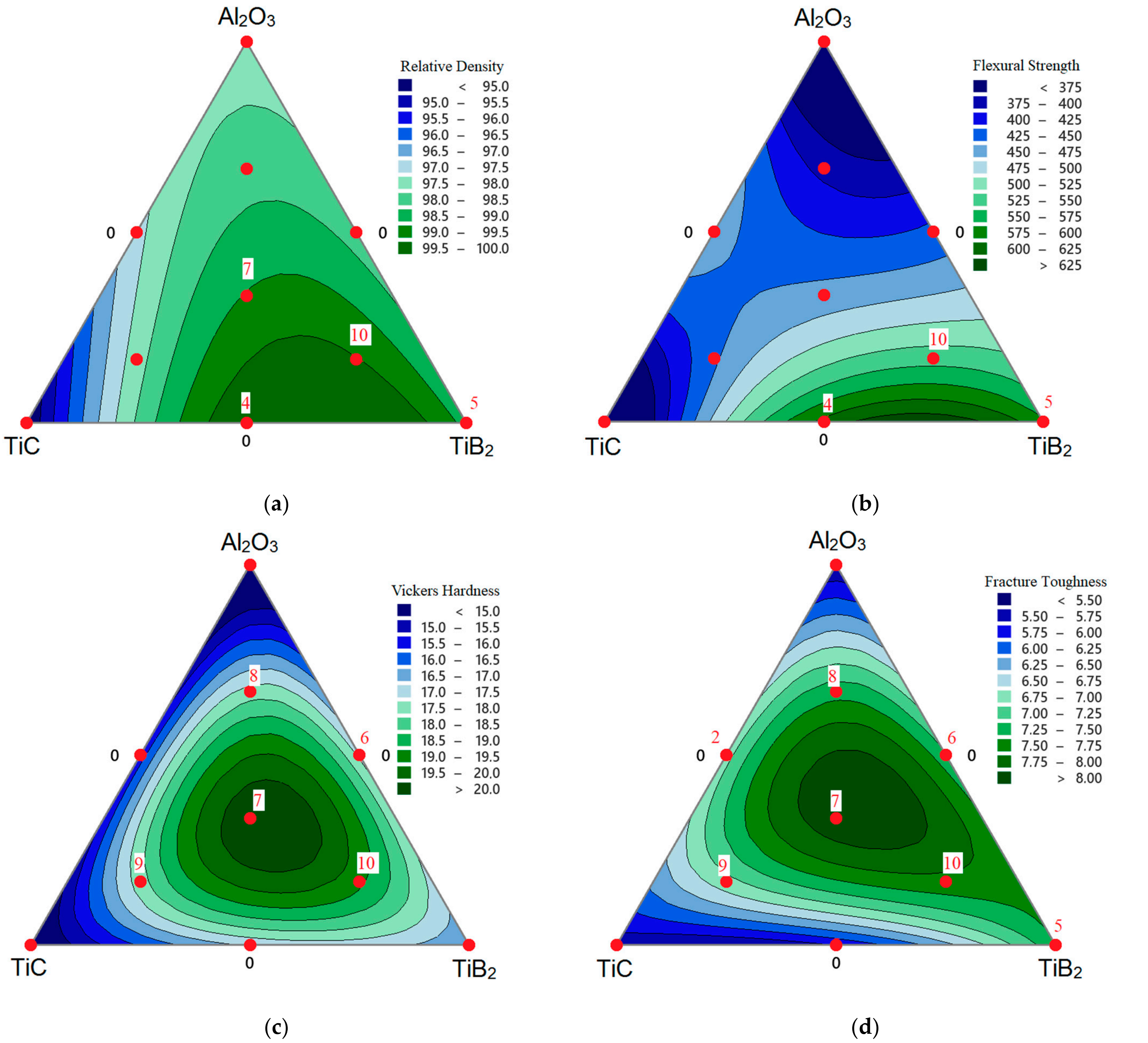

Figure 10. Contour plots in the Al_2O_3-TiB_2-TiC simplex: relative density (**a**), flexural strength (**b**), Vickers hardness (**c**), and fracture toughness (**d**) of sintered samples.

By combining the plots in Figure 8, it is possible to obtain one common zone in the Al_2O_3-TiB_2-TiC simplex, which can predict the following combination of physical and mechanical properties for the sintered composites by SPS at 1700 °C, 80 MPa, and dwell of 3 min: relative densities, flexural strength, Vickers hardness, and fracture toughness greater than 99%, 500 MPa, 18 GPa, and 7.00 MPa·m$^{1/2}$, respectively (Figure 11).

The models RD_Q, FS_{SC}., HV_{SC}, and FT_{SC} were additionally tested at three control points (Figure 11 points No. 11–13), the coordinates of which are given in Table 10.

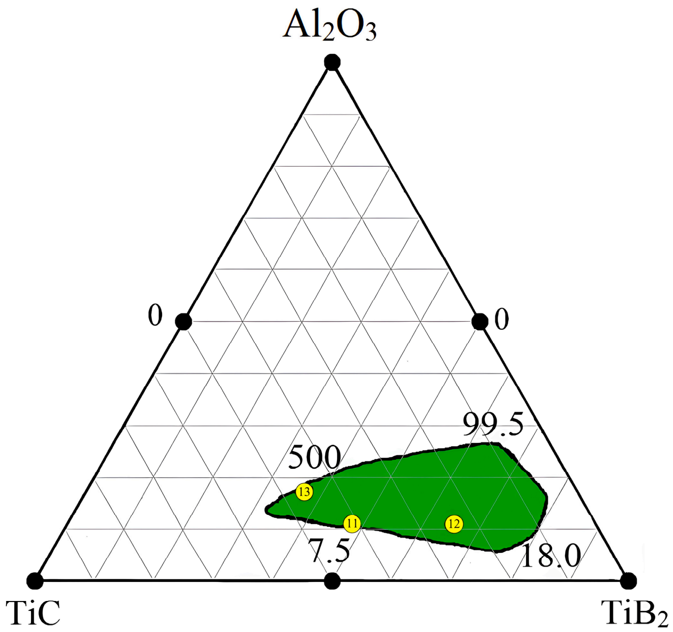

Figure 11. Zone in the Al2O3-TiB2-TiC simplex that corresponds to relative densities > 99%, flexural strength > 500 MPa, Vickers hardness > 18 GPa, and fracture toughness > 7.00 MPa·m1/2.

Table 10. Coordinates of control points in the ternary plot Al_2O_3–TiB_2–TiC.

Point	Al_2O_3	TiC	TiB_2	Mixture
No.		[mol %]		Name
11	11.1	40.3	48.6	2ATB-4
12	11.1	23.5	65.4	2ATB-5
13	16.7	46.0	37.3	2ATB-8

Table 11 shows the measured values of the relative density, flexural strength, Vickers hardness, and fracture toughness of sintered samples in the new three control points, as well as their predicted values, and confidence intervals.

Table 11. Comparison of experimental predicted data of test points.

Point	ρ_{rel} [%]		95%	σf [MPa]		95%	HV [GPa]		95%	K1c [MPa·m$^{1/2}$]		95%
No.	exp. *	pred. *	CI	exp. *	pred. *	CI *	exp. *	pred. *	CI *	exp. *	pred. *	CI *
11	99.57	99.77	(99.053; 100.491)	560	550.5	(498.2; 602.7)	19.03	19.16	(18.220; 20.108)	6.91	7.10	(6.549; 7.646)
12	99.49	99.85	(99.221; 100.479)	623	568.5	(523.6; 613.5)	18.93	18.93	(18.121; 19.741)	7.38	7.33	(6.858; 7.800)
13	98.77	99.30	(98.661; 99.933)	526	506.8	(453.2; 560.3)	18.85	19.56	(18.589; 20.530)	6.76	7.40	(6.838; 7.966)

*: exp.—experimental value; pred.—predicted value; CI—confidence interval.

From Table 11, it is clearly seen that experimental values fit well into the predicted intervals, except for the flexural strength in point No. 12. This can be related with the fact that the predicted R-squared value for the model FS_Q is 63.74%. The variation in predicted values for material relative density, flexural strength, and fracture toughness relative to experimental data shown in Table 11 can be explained by using the mean square pure error and residual error for each property and the chosen model. It is noticeable from Table 12 that the mean square residual errors of flexural strength and fracture toughness are approximately two times higher than the mean square pure error. Moreover, the mean square residual error of the relative density is approximately 2.5 times higher than the pure error. On the other hand, the error difference for Vickers hardness is smaller, and this explains the absence of a difference between the predicted and experimental data.

Table 12. Comparison of MSE for fitted and experimental values.

Mean Square	Relative Density	Flexural Strength	Vickers Hardness	Fracture Toughness
Pure error	0.3833	2443	1.333	0.2250
Residual error	0.9346	4589	1.475	0.4984

Despite these discrepancies in the experimental and fitted results, as a first approximation for determining the further direction of research, the selected models describe well the behavior of the studied properties of samples obtained by SPS at 1700 °C, 80 MPa, and a holding time of 3 min. Additionally, these results indicated that the design of mixture experiments is a simple and effective method for predicting, as a first approximation, physical and mechanical properties of ceramic composite materials with the use of only 10 different compositions for a composition of three components.

Moreover, in Table 13 are shown the theoretical densities of sintered composites in the three control points, as well as their measured and predicted values, and their confidence intervals. From this table, it is clearly seen that experimental values fit well into the predicted intervals.

Table 13. Theoretical and experimental density data of test points.

Point	$\rho_{th.}$ *	ρ * [g/cm^3]		95% CI *
No.	[g/cm^3]	exp.*	pred.*	
11	4.436	4.417	4.426	(4.394; 4.458)
12	4.369	4.347	4.362	(4.335; 4.390)
13	4.420	4.366	4.389	(4.361; 4.417)

*: $\rho_{th.}$—calculated theoretical density; ρ—measured density; exp.—experimental value; pred.—predicted value; CI—confidence interval.

These results indicated that the design of mixture experiments is a simple and effective method for predicting, as a first approximation, the physical and mechanical properties of ceramic composite materials with the use of only 10 different compositions for a composition of three components.

5. Conclusions

In this study, the design of mixture experiments was used to find empirical models that could predict, for a first approximation, the relative density, flexural strength, Vickers hardness, and fracture toughness of sintered composites in order to identify further areas of research in the Al_2O_3-TiB_2-TiC ternary system.

The composites were obtained by spark plasma sintering at 1700 °C, 80 MPa, and dwell of 3 min. The measured properties of sintered composites were analyzed in Minitab 17, and then different regression models were established for each property. Among the found models, four of them (RD_Q, FS_{SC}, HV_{SC}, and FT_{SC}) were selected for the prediction of the studied properties.

In this work, the evaluation of the selected models was provided by the use of the residual plots and fitted line plots. This evaluation showed that the models can predict, as a first approximation, the behavior of the studied properties.

Based on the selected models, contour plots were made in the Al_2O_3-TiB_2-TiC simplex for a visual representation of the predicted results. By combining these plots, it was possible to obtain one common zone in the simplex, which shows the combination of relative densities, flexural strength, Vickers hardness, and fracture toughness greater than 99%, 500 MPa, 18 GPa, and 7.0 $MPa \cdot m^{1/2}$, respectively.

Furthermore, the selected models were additionally tested at three control points in the established zone in the simplex. In these three points, the predicted values of relative density, flexural strength, and fracture toughness show a variation from the experimental data. It was demonstrated that this fact was related with the mean square errors of the models, which were higher than the mean square error of the experimental data.

Despite the fact that some fitted values were predicted with imperfect accuracy (for example, the fracture toughness), the selected empirical models allowed us to determine, for a first approximation, further areas of research. Moreover, the obtained results indicate that the design of mixture experiments is a simple and effective method for predicting the physical and mechanical properties of ceramic composite materials using a small number of different compositions.

The selected mathematical models work only for the prediction of properties of composites obtained by SPS within the specified sintering parameters and for the studied ceramic system.

In future work, the selected models will be refined in further extended studies conducted in the established area in the Al_2O_3-TiB_2-TiC simplex. A large number of mixtures will also be used and a more accurate model will be obtained. In addition, future work will include the study of microstructures to better understand mechanical characteristics.

Author Contributions: Conceptualization, N.W.S.P. and A.S.; methodology, N.W.S.P. and A.S.; software, Y.P. and Y.M.; validation, Y.M., N.L. and A.M.; formal analysis, Y.M. and A.M.; investigation, A.M., A.Y.K. and N.L.; resources, Y.P., Y.M. and N.L.; data curation, N.W.S.P. and Y.P.; writing—original draft preparation, N.W.S.P. and A.S.; writing—review and editing, N.W.S.P. and A.S.; visualization, A.Y.K. and Y.M.; supervision, A.S. and N.W.S.P.; project administration, N.W.S.P.; funding acquisition, N.W.S.P. All authors have read and agreed to the published version of the manuscript.

Funding: The work of N. W. Solís Pinargote, A. Smirnov, Y. R. Meleshkin, Nikolay Lavreshin, and Alexandra Yu. Kurmysheva was supported by the Russian Science Foundation (Grant Agreement No. 23-19-00413, https://rscf.ru/project/23-19-00413/ accessed on 28 October 2024).

Institutional Review Board Statement: Not applicable.

Informed Consent Statement: Not applicable.

Data Availability Statement: Data are contained within the article.

Acknowledgments: The authors would like to thank Nikita Nikitin (Spark Plasma Sintering Research Laboratory, Moscow State University of Technology "STANKIN", Russia) for his advice on data processing. This study was carried out on the equipment of the Center of Collective Use of MSTU "STANKIN" (project 075-15-2021-695).

Conflicts of Interest: Author Nikolay Lavreshin was employed by the company Microbor, SEZ Technopolis. The remaining authors declare that the research was conducted in the absence of any commercial or financial relationships that could be construed as a potential conflict of interest.

References

1. Grigoriev, S.N.; Pristinskiy, Y.; Soe, T.N.; Malakhinsky, A.; Mosyanov, M.; Podrabinnik, P.; Smirnov, A.; Solís Pinargote, N.W. Processing and Characterization of Spark Plasma Sintered SiC-TiB_2-TiC Powders. *Materials* **2022**, *15*, 1946. [CrossRef] [PubMed]
2. Stolin, A.M.; Bazhin, P.M.; Khairulina, R.V. Using the SHS extrusion process to produce composite nanoceramics. *Perspect. Mater.* **2012**, *2*, 77–82. (In Russian)
3. Sahu, J.K.; Sahoo, C.K.; Masanta, M. In-Situ TiB_2–TiC–Al_2O_3 Composite Coating on Aluminum by Laser Surface Modification. *Mater. Manuf. Process.* **2015**, *30*, 736–742. [CrossRef]
4. Zou, B.; Huang, C.; Ji, W.; Li, S. Effects of Al_2O_3 and NbC additives on the microstructure and mechanical properties of TiB_2–TiC composite ceramic cutting tool materials. *Ceram. Int.* **2014**, *40*, 3667–3677. [CrossRef]
5. Chen, Z.; Ji, L.; Guo, N.; Xu, C.; Zhang, S. Crack healing and strength recovery of Al_2O_3/TiC/TiB_2 ceramic tool materials. *Int. J. Refract. Met. Hard Mater.* **2020**, *87*, 105167. [CrossRef]

6. Cui, H.; Chen, Z.; Xiao, G.; Ji, L.; Yi, M.; Zhang, J.; Zhou, T.; Xu, C. Mechanical Proper-ties and Microstructures of Al_2O_3/TiC/TiB_2 Ceramic Tool Material. *Crystals* **2021**, *11*, 637. [CrossRef]
7. Wang, D.; Bai, Y.; Qiu, B.; Yu, H.; Li, Z. Design of spark plasma sintering parameters and preparation of Al_2O_3/TiB_2/TiC micro–nano composite ceramic tool material. *Int. J. Appl. Ceram. Technol.* **2022**, *20*, 1420. [CrossRef]
8. Cui, X.; Li, Y.; Guo, J.; Guo, Q. Fabrication, transport behaviors and green interrupted cutting performance of bio-inspired microstructure on Al_2O_3/TiC composite ceramic surface. *J. Manuf. Process.* **2022**, *75*, 203–218. [CrossRef]
9. Aydin, H.; Elmus, B. Fabrication and characterization of Al_2O_3-TiB_2 nano-composite powder by mechanochemical processing. *J. Aust. Ceram. Soc.* **2021**, *57*, 731–741. [CrossRef]
10. Matsuda, T. Synthesis and sintering of TiC-TiB_2 composite powders. *Mater. Today Commun.* **2020**, *25*, 101457. [CrossRef]
11. Zou, B.; Shen, P.; Cao, X.; Jiang, Q. Reaction path of the synthesis of α-Al_2O_3-TiC-TiB_2 in an Al-TiO_2-B_4C system. *Int. J. Refract. Met. Hard Mater.* **2011**, *29*, 591–595. [CrossRef]
12. Xu, J.; Zou, B.; Fan, X.; Zhao, S.; Hui, Y.; Wang, Y.; Zhou, X.; Cai, X.; Tao, S.; Ma, H.; et al. Reactive plasma spraying synthesis and characterization of TiB_2–TiC–Al_2O_3/Al composite coatings on a magnesium alloy. *J. Alloys Compd.* **2014**, *596*, 10–18. [CrossRef]
13. Li, Z.; Wei, M.; Xiao, K.; Bai, Z.; Xue, W.; Dong, C.; Wei, D.; Li, X. Microhardness and wear resistance of Al_2O_3-TiB_2-TiC ceramic coatings on carbon steel fabricated by laser cladding. *Ceram. Int.* **2018**, *45*, 115–121. [CrossRef]
14. Masanta, M.; Ganesh, P.; Kaul, R.; Roy Choudhury, A. Microstructure and mechanical properties of TiB_2–TiC–Al_2O_3–SiC composite coatings developed by combined SHS, sol–gel and laser technology. *Surf. Coat. Technol.* **2010**, *204*, 3471–3480. [CrossRef]
15. Wang, Z.; Liu, X.; Bian, X. Reaction in the Al-TiO_2-CB_4 System andin Situ Synthesis of an Al/(TiC + TiB_2 + $\alpha - Al_2O_3$) Composite. *Adv. Eng. Mater.* **2004**, *6*, 977–980. [CrossRef]
16. Akao, T.; Tonoko, K.; Onda, T.; Chen, Z.-C. In-situ Synthesis of Al-based Composites Reinforced with TiB_2-TiC-Al_2O_3 Ceramic Particulates. *J. Sustain. Res. Eng.* **2015**, *2*, 45–52.
17. Like, Q.; Xikun, L.; Yang, P.; Weimin, M.; Guanming, Q.; Yanbin, S. Types, Performance and Application of AI_2O_3 System Ceramic Cutting Tool. *J. Rare Earths* **2007**, *25*, 322–326. [CrossRef]
18. Gong, F.; Zhao, J.; Liu, G.; Ni, X. Design and fabrication of TiB_2–TiC–Al_2O_3 gradient composite ceramic tool materials reinforced by VC/Cr3C2 additives. *Ceram. Int.* **2021**, *47*, 20341–20351. [CrossRef]
19. Fernandez-Garcia, E.; Gutierrez-Gonzalez, C.F.; Peretyagin, P.; Solis, W.; Lopez-Esteban, S.; Torrecillas, R.; Fernandez, A. Effect of yttria–titanium shell–core structured powder on strength and ageing of zirconia/titanium composites. *Mater. Sci. Eng. A* **2015**, *646*, 96–100. [CrossRef]
20. Díaz, L.A.; Solís, W.; Peretyagin, P.; Fernández, A.; Morales, M.; Pecharromán, C.; Moya, J.S.; Torrecillas, R. Spark Plasma Sintered Si_3N_4/TiN Nanocomposites Obtained by a Colloidal Processing Route. *J. Nanomater.* **2016**, *2016*, 3170142. [CrossRef]
21. Yushin, D.I.; Smirnov, A.V.; Solis Pinargote, N.; Peretyagin, P.Y.; Kuznetsov, V.A.; Torrecillas, R. Spark plasma sintering of cutting plates. *Russ. Eng. Res.* **2016**, *36*, 410–413. [CrossRef]
22. Gutiérrez-González, C.F.; Pozhidaev, S.; Rivera, S.; Peretyagin, P.; Solís, W.; Díaz, L.A.; Fernández, A.; Torrecillas, R. Longer-lasting Al_2O_3-SiCw-TiC cutting tools obtained by spark plasma sintering. *Int. J. Appl. Ceram. Technol.* **2017**, *14*, 367–373. [CrossRef]
23. Yushin, D.I.; Smirnov, A.V.; Pinargote, N.W.S.; Peretyagin, P.Y.; Millan, R.T.S. Modeling Process of Spark Plasma Sintering of Powder Materials by Finite Element Method. *Mater. Sci. Forum* **2015**, *834*, 41–50. [CrossRef]
24. Pristinskiy, Y.; Pinargote, N.W.S.; Smirnov, A. The effect of MgO addition on the microstructure and mechanical properties of alumina ceramic obtained by spark plasma sintering. *Mater. Today Proc.* **2019**, *19*, 1990–1993. [CrossRef]
25. Pristinskiy, Y.; Pinargote, N.W.S.; Smirnov, A. Spark plasma and conventional sintering of ZrO_2-TiN composites: A comparative study on the microstructure and mechanical properties. *MATEC Web Conf.* **2018**, *224*, 01055. [CrossRef]
26. Solvason, C.; Chemmangattuvalappil, N.G.; Eljack, F.T.; Eden, M.R. Efficient Visual Mixture Design of Experiments using Property Clustering Technique. *Ind. Eng. Chem. Res.* **2009**, *48*, 2245–2256. [CrossRef]
27. Cornell, J.A. *A Primer on Experiments with Mixtures*; Wiley Series in Probability and Statistics; John Wiley & Sons, Inc.: Hoboken, NJ, USA, 2011.
28. de Mestral, F.; Thevenot, F. Boride-Carbide Composites: TiB_2-TiC-SiC. In *The Physics and Chemistry of Carbides, Nitrides and Borides*; Freer, R., Ed.; NATO ASI Series; Springer: Dordrecht, The Netherlands, 1990; Volume 185. [CrossRef]
29. de Mestral, F.; Thevenot, F. Ceramic composites: TiB_2-TiC-SiC. Part I Properties and microstructures in the ternary system. *J. Mater. Sci.* **1991**, *26*, 5547–5560. [CrossRef]
30. de Mestral, F.; Thevenot, F. Ceramic composites: TiB_2-TiC-SiC. II: Optimization of the composite 20% TiB_2-55% (mol %) TiC-25% SiC. *J. Mater. Sci.* **1991**, *26*, 5561–5565. [CrossRef]
31. Coronado, M.; Segadães, A.M.; Andrés, A. Combining mixture design of experiments with phase diagrams in the evaluation of structural ceramics containing foundry by-products. *Appl. Clay Sci.* **2014**, *101*, 390–400. [CrossRef]
32. Silveira, J.; Leite, J.P. Technique for optimization of ceramic bodies using mixture design. *Ceramica* **2010**, *56*, 347–354. [CrossRef]
33. Khaskhoussi, A.; Calabrese, L.; Bouhamed, H.; Kamoun, A.; Proverbio, E.; Bouaziz, J. Mixture design approach to optimize the performance of TiO_2 modified zirconia/alumina sintered ceramics. *Mater. Des.* **2018**, *137*, 1–8. [CrossRef]

34. Rajendar, K.; Eswaraiah, K. Experimental investigation and optimization for friction and wear behavior of aluminum LM 25/h-BN/B_4C composites via mixture design and desirability approach. *Int. J. Interact. Des. Manuf.* **2024**, *18*, 2017–2029. [CrossRef]
35. *21-ASTM C1161-13*; Standard Test Method for Flexural Strength of Advanced Ceramics at Ambient Temperature. ASTM International: West Conshohocken, PA, USA, 2013.